CARBON 87 (2015) 193–205

Available at www.sciencedirect.com

ScienceDirect

journal homepage: www.elsevier.com/locate/carbon

Micro/nano-structured graphitic carbon nitride–Ag nanoparticle hybrids as surface-enhanced Raman scattering substrates with much improved long-term stability

Jizhou Jiang [a,b], Lihua Zhu [a], Jing Zou [c], Lei Ou-yang [a,b], Anmin Zheng [d], Heqing Tang [b,*]

[a] College of Chemistry and Chemical Engineering, Huazhong University of Science and Technology, Wuhan 430074, PR China
[b] Key Laboratory of Catalysis and Materials Science of the State Ethnic Affairs Commission and Ministry of Education, College of Chemistry and Materials Science, South Central University for Nationalities, Wuhan 430074, PR China
[c] School of Chemistry and Environmental Engineering, Key Laboratory for Green Chemical Process of Ministry of Education, Wuhan Institute of Technology, Wuhan 430073, PR China
[d] State Key Laboratory of Magnetic Resonance and Atomic and Molecular Physics, Wuhan Institute of Physics and Mathematics, Chinese Academy of Sciences, Wuhan 430071, PR China

ARTICLE INFO

Article history:
Received 23 November 2014
Accepted 4 February 2015
Available online 11 February 2015

ABSTRACT

Surface-enhanced Raman scattering (SERS) substrates with high SERS activity and stability are important for SERS sensors. A facile method was developed to fabricate efficient and stable SERS substrates by combining Ag nanoparticles (NPs) and micro-scale sheeted graphitic carbon nitride (g-C_3N_4). The g-C_3N_4/Ag NPs hybrid could provide a great number of hot spots and concentrated the analyte by the π–π stacking interaction between analyte molecules and g-C_3N_4, making a dramatic Raman enhancement. Moreover, the g-C_3N_4/Ag NPs hybrid uniformly immobilized Ag NPs on the surface and edges of g-C_3N_4 sheets by an interaction between Ag NPs and g-C_3N_4, leading to much improved long-term stability. This could be explained in terms of the electron–donor effect of g-C_3N_4, which was further confirmed by density functional theory calculations. The inherent Raman enhancing effect of g-C_3N_4 itself also contributed to the total SERS responses. Due to multiple enhancement contributions, the g-C_3N_4/Ag NPs hybrid exhibited a strong Raman enhancement effect for with an enhancement factor of 4.6×10^8 (evaluated by using crystal violet as a probe), and possessed wide adaptability from dyes, pesticides to bio-molecules.

1. Introduction

Surface enhanced Raman scattering (SERS) is a powerful spectroscopic technique that can detect trace amounts of analytes and identify them based on their unique Raman vibrational spectroscopic fingerprints [1–3]. The SERS field has dramatically progressed from the first observed enhancement on roughened silver electrodes [4] to the current fields of explosives detection [5,6], food safety and security [2,7,8], live-cell imaging [9], cancer marker detection [10], and art

* *Corresponding author.*
E-mail addresses: tangheqing@mail.scuec.edu.cn, hqtang62@aliyun.com (H. Tang).
http://dx.doi.org/10.1016/j.carbon.2015.02.025
0008-6223/

identification [11]. The current understanding of SERS phenomena holds two primary theoretical models: long-range electromagnetic enhancement and short-range chemical enhancement, and electromagnetic enhancements make a major contribution to the SERS phenomenon [12,13]. An incident laser light, when properly matched to the nanoscale geometry and material that define the SERS substrate, excites the localized surface plasmons on the metal. This leads to redistribution of the local field and a great enhancement of the electromagnetic field at a specific position around the NPs (called "hot spots"). There are also reports of chemical enhancement, charge transfer between chemisorbed molecules and a metal surface, which provides Raman enhancement by one or two orders of magnitude [14].

Since substrate materials play key roles in SERS, researchers strived to develop new substrates and optimize their structures and configurations. The earliest reported SERS substrates are Au, Ag and Cu roughened electrodes [15,16]. Later, colloidal Au and Ag NPs are widely employed in SERS for several decades, because they have advantages of tunable particle sizes and shapes. However, Ag NPs colloids suffer from problems including poor stability and reproducibility due to colloid aggregation [17]. Recently, graphene oxide (GO), a single layer of carbon atoms network, has attracted much attention because of its fascinating properties and potential applications [18,19]. The oxygen-containing donor sites on the surface of GO, such as carboxylic acid groups at the sheet edges and hydroxyl and epoxy groups on the graphitic plane [20,21], are easy to operate metals NPs, resulting in that the NPs are grown on the surface without aggregation. Huang [22] and Qin and co-workers [23] reported Au–GO nanohybrids as SERS substrates, and found that the Au/GO hybrids were superior to Au NPs. Saha and co-workers [24] reported a way of generating stable electromagnetic hot spots from colloidal Ag/Au NPs and GO. Fan and co-workers [25] found that the Ag@GO nanostructures consisting of Ag NPs assembled on GO sheets could yielded SERS intensities being 2–3 times that produced by pure Ag NPs.

Nonetheless, the decrease in the number of oxygen-rich species on GO sheets in GO/metals NPs materials caused a decrease in SERS signals. It was reported that the enhancement factor was decreased by 35% on Ag@reduced GO (RGO) (with 10 atomic% oxygen on RGO sheets) in comparison with that on Ag@GO (with 40 atomic% oxygen) [25]. Moreover, GO/metal NPs hybrids are often unstable under ambient conditions. The GO/Au NPs composites, which were prepared by noncovalent attachment of Au NPs premodified with 2-mercaptopyridine to GO sheets, were only stable for two week [22]. It was reported that the SERS signal on the GO/Ag (Au) NPs aggregation remained stable only for 3 days under ambient conditions [24]. Gupta and co-workers [26] reported that Ag@AuNPs–GO composite was only stable just for 12 h. The unstable SERS activity originates mainly from the oxidation of metal NPs on the surface of GO sheets [27]. Therefore, it remains highly desirable to develop an effective approach of preparing SERS substrate materials with much higher stability.

As an analogue of graphite, graphitic carbon nitride (g-C_3N_4) possesses a stacked 2D structure, which can be regarded as an N-substituted graphite framework consisting of π-conjugated graphitic planes formed via sp^2 hybridization of carbon and nitrogen atoms [28]. g-C_3N_4 is a promising candidate to complement carbon in materials applications. Although the history of carbon nitride and its precursors started in the very early days of Berzelius and Liebig in 1834 [29], it is recent years that carbon nitride attract much attention due to the theoretical prediction of their unique electronic properties, remarkable mechanical properties and wide promising applications [30–33] in fields of energy conversion and storage [34], water splitting [35–37], CO_2 capture [38], organic catalysis [39,40] and pollution control [41–43]. It can be produced on a large scale with low cost by bulk condensation of N-rich precursors including urea, cyanamide and melamine [44]. We have recently investigated the electronic structure of 1-, 2-, and 4-layer g-C_3N_4 nanosheets by combining Raman spectra and the first-principles calculations, and clarified a clear correlation between the spectral properties and the layer number of the nanosheets [45]. Based on our experiences, the combination of g-C_3N_4 and metals NPs may create good SERS substrates, because noble metals NPs supply strong SERS activity and g-C_3N_4 can concentrate the target molecules. Meanwhile, the atomic content of N is close to 60% in g-C_3N_4, and the N atoms are distributed in each atomic layer, not just on the surface of bulky g-C_3N_4 materials, where the strong coordinating ability of N could be favorable to increasing the stability of g-C_3N_4/metals NPs hybrids. As SERS substrates, g-C_3N_4/metals NPs hybrids would display high SERS performance.

Therefore, we prepared a g-C_3N_4/Ag NPs hybrid and showed its strong SERS activity both in the enhancement effect and in the long-term stability. By using crystal violet as a probe, the g-C_3N_4/Ag NPs substrate material was confirmed to provide an enhancing factor as high as 4.6×10^8 in comparison with normal Raman scattering. The g-C_3N_4/Ag NPs substrate had wide adaptability for organic compounds such as dyes, pesticides and bio-molecules with crystal violet (CV, $C_{25}H_{30}ClN_3$), paraquat (1,1′-dimethyl-4,4′-bipyridinium dimethosulfate, $C_{12}H_{14}Cl_2N_2$) and guanine (2-amino-1H-purin-6(9H)-one, $C_5H_5N_5O$) as their corresponding representatives. Especially, the hybrid substrates exhibited excellent long-term stability. These ensure that the hybrid substrates have promising applications in routine SERS analysis of organic pollutants and biomolecules.

2. Experimental

2.1. Reagents and materials

Melamine ($C_3N_3(NH_2)_3$), silver nitrate ($AgNO_3$), sodium hydroxide (NaOH), and hydroxylamine hydrochloride (NH_2-OH·HCl) were purchased from Sinopharm Chemical Reagent Co. Ltd. Guanine and p-aminothiophenol (PATP, C_6H_7NS) were obtained from Aladdin Chemical Co. Ltd. Paraquat was purchased from Hubei Sanonda Co. Ltd. Tianmen Agrochemical Plant. CV from Sigma–Aldrich was used as Raman probes. All the chemicals were of analytical grade and were used as received. Milli-Q water (18.2 MΩ cm) provided by a Milli-Q Labo apparatus (Thermo Fischer Scientific) was used in all experiments.

2.2. Characterization

Transmission electron microscopy (TEM) images and the energy dispersive spectra (EDS) were recorded on a TECNAI G2 20U-Twin electron microscope, using an accelerating voltage of 200 kV. Samples for TEM analysis were prepared by drying a drop of nanocrystal dispersion in absolute ethanol on carbon-coated copper grids. The particle size was measured on a Nano-ZS90 zetasizer instrument (Malvern). The crystallinity was determined on a Bruker D8 Advance TXS X-rays diffractometer (XRD) equipped with Cu Kα radiation (λ = 1.54 Å) source (applied voltage 40 kV, current 40 mA). Scans were recorded for 2θ values between 10° and 80°, using a step size of 0.02° and integration of 16 s per step. UV–visible absorption spectra were recorded on a Shimadzu UV-2550 spectrophotometer (Kyoto, Japan). Emission spectra were obtained by a FP-6200 fluorescence spectrophotometer (Jasco). X-ray photoelectron spectroscopic (XPS) analysis was conducted on a VG Multilab 2000 spectrometer (Thermo Electron Corporation) with Al Kα radiation as the exciting source (300 W). During the measurement, the sample was supported on a copper substrate. The binding energies of recorded XPS spectra were corrected according to C 1s line at 284.61 eV. After subtracting the Shirley-type background, the core-level spectra were decomposed into their components with mixed Gaussian–Lorentzian (20:80) shapelines using the CasaXPS software. Raman spectra were measured on a confocal laser micro-Raman spectrometer (Thermo Fischer DXR) equipped with a diode laser of excitation of 532 nm (laser serial number: AJC1200566). The laser was focused onto the substrate with an Olympus ×50 long distance objective. The radius of illumination laser spot size was ~0.55 μm. Samples were mounted on an automatic stage allowing the control of 1 μm step size. Spectra were obtained at a laser output power of 1 mW (532 nm), and a 0.2 s acquisition time with 900 lines/mm grating (Grating serial number: AJG1200531) in the wavenumber range of 50–3500 cm^{-1}. Baseline corrections were carried out to correct the optical background signal from the substrate. Both brightfield and darkfield illumination modes were used to visually analyze the samples in preparation for data collection. Data collection, processing, and analysis was performed using the Thermo Scientific OMNIC software suite, including OMNIC™ Atlμs™. Raman mapping was performed on a latest Thermo Fisher Scientific DXRxi Raman imaging microscope.

For SERS analysis, the g-C_3N_4/Ag hybrid suspension was firstly shaken for several minutes to obtain a uniform dispersion. In the SERS measurements by using CV as the probe, 0.1 mL of the hybrid dispersion and 2 mL of CV solution (2.5×10^{-6} mol L^{-1}) were mixed together, followed by shaking for 5 min. The mixture (10 μL) was finally dropped onto a clean glass slide for the measurement. Other analytes were also detected similarly.

2.3. Preparation of SERS substrates

At first, g-C_3N_4 was prepared by polymerization of melamine under air [45,46]. Briefly, a ceramic crucible loaded with 4 g of melamine powder was placed into the centre of a muffle furnace. The furnace was gradually heated to 520 °C at a rate of 10 K min^{-1} and held at this temperature for 4 h. After cooling the furnace to room temperature a yellow-colored product was found in the downstream region of the ceramic crucible. The obtained product was characterized as bulk g-C_3N_4 powders.

Secondly, Ag NPs were prepared by the hydroxylamine hydrochloride reduction method [47]. Typically, 40 mL of NaOH solution (7.5 mmol L^{-1}) was added to 50 mL of the NH_2-OH·HCl solution (3.0 mmol L^{-1}) under ultrasound irradiation. Then 10 mL of $AgNO_3$ aqueous solution (10 mmol L^{-1}) was rapidly added to the mixture under ultrasound irradiation with a powder of 140 W. After 5 min, a milky gray color colloid was obtained and stored in a refrigerator at 4 °C prior to use.

Finally, g-C_3N_4/Ag hybrids were prepared. To prepare the hybrids, bulk g-C_3N_4 powders (0.02 g) were added in 20 mL of Ag NPs colloid under vigorous stirring at room temperature. After stirred for 1 h, aliquots of the mixture were transferred into 5 mL microcentrifuge tubes and centrifuged at 5000 rpm for 5 min. The precipitates from each tube were redispersed in 5 mL of Milli-Q water. The resultant dispersion was stored at ambient temperature prior to use.

2.4. Computational details

The geometry structure and electronic properties of target molecules were performed using Gaussian09 software package [48]. Optimization of the molecular structures were performed by means of density functional theory (DFT) with the Becke's 3 parameters and the Lee–Yang–Parr's nonlocal correlation functional (B3LYP). The basis sets for C, N and H were 6-31+G (d) with diffuse function for N and O atoms. In the case of the g-C_3N_4–silver complexes, a mixed basis set (6-31+G-(d) for all atoms except silver, LanL2DZ was employed for silver) was used.

The geometry and electronic structure of g-C_3N_4 were analyzed by the plane-wave ultrasoft (PWUS) pseudopotential method as implemented in the Cambridge Sequential Total Energy Package (CASTEP) code [49]. The calculation was also performed using the PWUS pseudopotential method with the local density approximation (LDA) functional of Ceperley and Alder as parameterized by Perdew and Zunger (CAPZ) [50]. In PWUS calculations, a hybrid semiempirical solution (OBS) was taken to introduce damped atom pairwise dispersion corrections of the form $C6R^{-6}$ in the DFT formalism. The valence atomic configurations are $2s^22p^2$ for C, $2s^22p^3$ for N. A cutoff energy of 600 eV and a Monkhorst–Pack k-mesh of 4 × 4 × 4 is used. The self-consistent convergence accuracy was set at 4×10^{-6} eV/atom. The convergence criterion for the maximal force on atoms is 0.02 eV/Å. The maximum displacement is 5×10^{-4} Å, and the stress is less than 0.02 GPa. The Raman vibrational analysis of primitive g-C_3N_4 was performed by CASTEP calculation.

3. Results and discussion

3.1. Preparation and characterization of g-C_3N_4/Ag NPs substrates

As expressed in the Introduction, we aimed at preparing a g-C_3N_4/Ag NPs micro/nano-structured hybrid for its good SERS

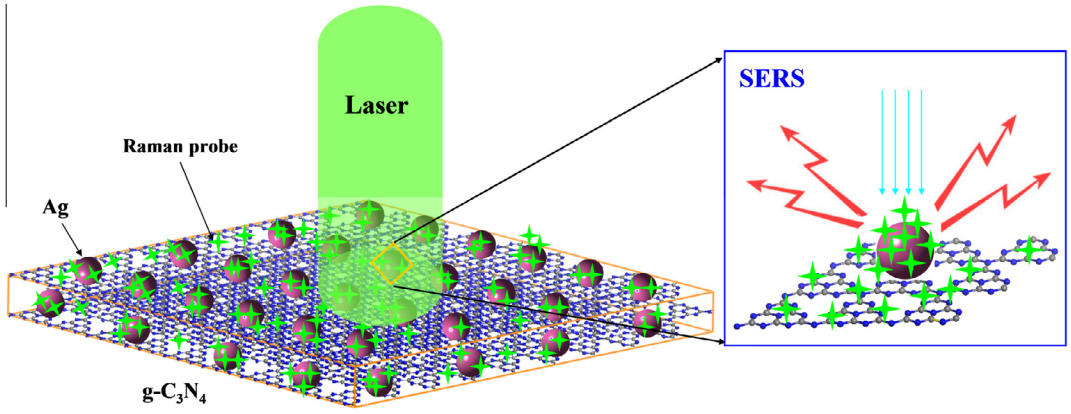

Fig. 1 – Schematic illustration of the micro/nanostructure of the g-C_3N_4/Ag NPs hybrid and its use for SERS detection of the probe molecules. (A colour version of this figure can be viewed online.)

activity and long-term stability. Fig. 1 showed a schematic illustration of the micro/nano structure of the g-C_3N_4/Ag NPs hybrid and its use for SERS detection of the probe molecules. In this hybrid, the target molecules (aromatic molecules) are strongly adsorbed on the surfaces of g-C_3N_4 sheets, due to the π–π interaction between aromatic molecules and g-C_3N_4 [51]. Meanwhile, because of the covalent bonding and electrostatic interactions between Raman probe molecules and Ag NPs [47], the target molecules are also strongly adsorbed on the surrounding of Ag NPs. The uniform immobilization of Ag NPs on the surface of g-C_3N_4 will eliminate the Brownian movement of Ag NPs, providing a better reproducibility in the measurement. Moreover, the g-C_3N_4/Ag NPs hybrid was much more resistant to oxidation than the separated Ag NPs, due to the charge transfer from the highest-occupied molecular orbital (HOMO) of g-C_3N_4 to the lowest-unoccupied molecular orbital (LUMO) of Ag NPs. Thus, the hybrid will have high SERS performances. Meanwhile, as an organic semiconductor consists of carbon and nitrogen, g-C_3N_4 is environmentally friendly and can be produced on a large scale with low cost by bulk condensation of N-rich precursors [44]. Moreover, the fabrication method of the g-C_3N_4/Ag hybrid substrate was simple and does not require additional training in sample preparation and handling. Therefore, the g-C_3N_4/Ag hybrid substrate has the merits of low cost and high availability.

Ag NPs, g-C_3N_4 and g-C_3N_4/Ag NPs hybrid were prepared and characterized. The TEM image of Ag NPs (Fig. 2a) clearly illustrated the as-prepared colloidal Ag NPs were monodisperse with an average diameter of about 40 nm, being in agreement with the result obtained from the size distribution of colloidal Ag NPs (41.8 nm, Fig. 2d). It was seen from Fig. 2b that the powders presented in the form of micrometer-sized sheets. In the g-C_3N_4/Ag NPs hybrid, Ag NPs were uniformly immobilized on the surface and edges of g-C_3N_4 sheets (Figs. 2c and S1 in Supporting information (SI)). The g-C_3N_4 and g-C_3N_4/Ag NPs hybrid powders were also characterized by XRD (Fig. 2e). In the XRD pattern of g-C_3N_4, the (002) peak at $2\theta = 27.3°$ reflected the characteristic interlayer stacking structure, while the (100) diffraction at 13.1° indicated the interplanar structural packing [46], indicating that the layer-structured g-C_3N_4 was successfully synthesized. In the XRD pattern of g-C_3N_4/Ag NPs hybrid, in addition to the two characteristic peaks of g-C_3N_4, the (111) peak at 38.1°, the (200) peak at 44.3°, the (220) peak at 64.4°, the (311) peak at 77.5° were all the characteristic peaks for the cubic Ag crystal (JCPDS Card No. 04-0783), suggesting successfully preparation of the g-C_3N_4/Ag hybrid. In addition, the successful synthesis of Ag NPs, g-C_3N_4 and g-C_3N_4/Ag hybrid was further evidenced by their EDS analysis (Fig. S2 in SI).

3.2. SERS activity of g-C_3N_4/Ag NPs substrates

To examine the Raman activity of the g-C_3N_4/Ag hybrid substrate, the operation parameters of the measurement were pre-optimized by using CV (2.5×10^{-6} mol L^{-1}) as a probe (Figs. S3–S5 in SI). The intensity and resolution of Raman vibrational peaks were used as the standards in the measurements for pre-optimization. Under the optimized conditions (the laser output power: 1 mW; sample exposure times: twice; collect exposure time: 0.2 s), it was easy to obtain satisfactory Raman signal intensities. The load of Ag NPs in the g-C_3N_4/Ag hybrid also showed strong influences on SERS enhancing ability of the substrate. By checking the SERS spectra of CV on the substrate being prepared with different amounts of g-C_3N_4 and Ag colloid (Fig. S6 in SI), it was observed the Raman intensity increased with decreasing the mass ratio of g-C_3N_4 to Ag colloid, suggesting that greater number of Ag NPs on the surface of g-C_3N_4 sheets induced more hot spots for strong localized electromagnetic fields. Hence, the mass ratio of g-C_3N_4 (mg) to Ag colloid (mL) was chosen at 1:1 for the next experiments.

Quantification of the enhancement factor (EF) of a SERS substrate needs some assumptions since the number of adsorbed molecules is poorly defined. In this work, we assume that probe molecules are uniformly adsorbed on the SERS substrates surface. EF was calculated by using the standard formula [47]:

$$EF = I_{SERS} * C_{NR}/I_{NR} * C_{SERS}$$

where I_{SERS} and I_{NR} are the integral intensity obtained by SERS and normal Raman scattering measurements, respectively. C_{SERS} and C_{NR} are the concentration of molecules used for SERS and normal Raman scattering measurements, respec-

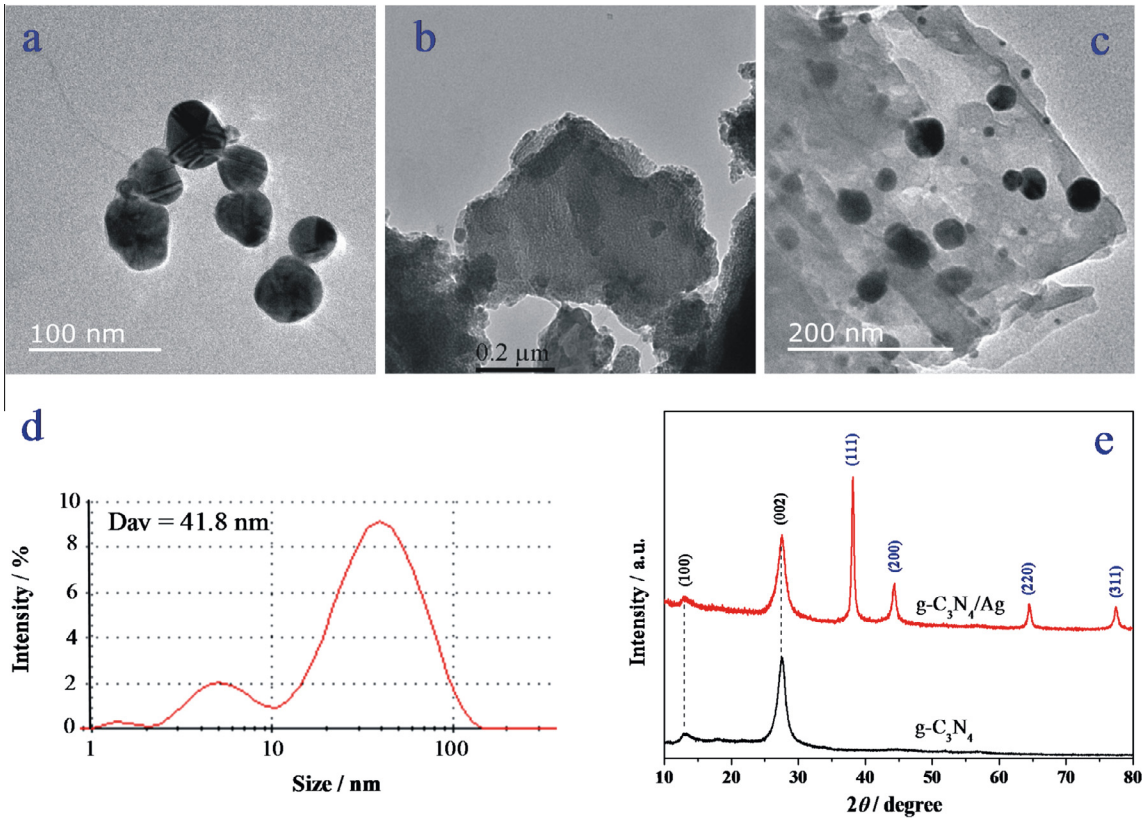

Fig. 2 – TEM images of (a) colloidal Ag NPs, (b) g-C_3N_4, (c) g-C_3N_4/Ag NPs hybrid, (d) the size distribution of colloidal Ag NPs, and (e) XRD patterns of g-C_3N_4 and g-C_3N_4/Ag. (A colour version of this figure can be viewed online.)

tively. The most intense peak was considered for EF calculation, and the EF values of different substrates were obtained (Table S1 in SI). For a more comprehensive estimation of EF, we utilize the average intensity from 20 sampling points of the substrate.

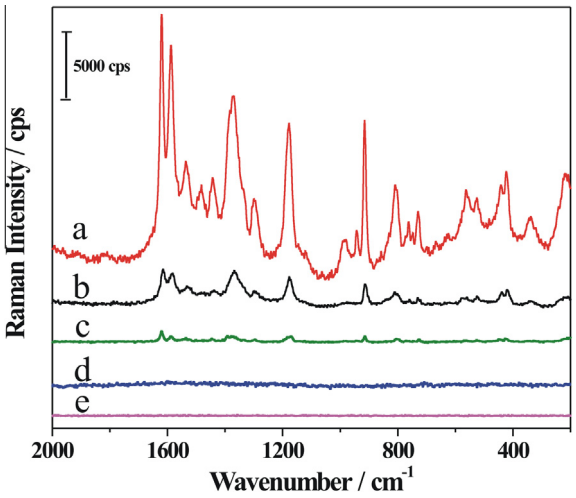

Fig. 3 – SERS spectra of CV (2.5×10^{-6} mol L^{-1}) on (a) g-C_3N_4/Ag, (c) Ag NPs colloid and (d) g-C_3N_4. The normal Raman spectra of (b) CV powder and (e) CV solution (2.5×10^{-6} mol L^{-1}) were given for comparison. (A colour version of this figure can be viewed online.)

Fig. 3 compared the SERS spectra of CV on different substrates. The normal Raman spectrum of CV powder (Fig. 3b) was used as the reference for the peak position in SERS measurement. Obviously, no Raman signal of CV solution was observed (Fig. 3e), and little SERS responses of CV were observed on the g-C_3N_4 substrate (Fig. 3d). Weak responses with very limited characteristic peaks of CV were produced on the Ag NPs substrate (Fig. 3c). However, all the characteristic Raman peaks are significantly enhanced in intensity on the g-C_3N_4/Ag substrates (Fig. 3a), demonstrating a strong Raman enhancement effect on the g-C_3N_4/Ag hybrid. The calculations of the enhancement factor (Table S1 in SI) showed that the g-C_3N_4/Ag NPs substrate provided an enhancing factor as high as 4.6×10^8, being much greater than that provide by individual Ag NPs colloid (3.1×10^6) as a control. Meanwhile, this g-C_3N_4/Ag NPs substrate also showed intense enhancement of Raman signals of PATP with an enhancement factor of 8.3×10^8 (Fig. S7 in SI), being superior to previously reported results [22,52]. These results imply that the g-C_3N_4/Ag hybrid can work effectively for SERS detection.

3.3. *Reproducibility, stability, uniformity and wide adaptability of g-C_3N_4/Ag NPs substrate*

The reproducibility, stability and uniformity of the substrate are important parameters for SERS detection. To evaluate the reproducibility of the substrates, SERS spectra of CV were measured by using ten batches of g-C_3N_4/Ag hybrid substrates prepared under the same conditions. As shown in Fig. 4, the

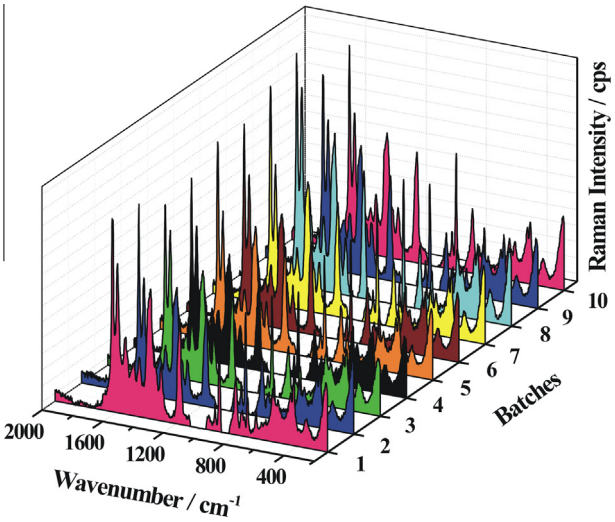

Fig. 4 – SERS spectra of CV (2.5×10^{-6} mol L^{-1}) on ten batches of g-C_3N_4/Ag NPs substrates prepared under the same conditions. (A colour version of this figure can be viewed online.)

spectra from the ten different-batch substrates overlapped very well. The relative standard deviations (RSD%) of the Raman intensity at 1619 cm^{-1} was only 9.9%. This indicates that the g-C_3N_4/Ag hybrid substrates exhibit good reproducibility.

A good SERS substrate is required to have high long-term stability during its storing. Any aggregation or oxidation of metal NPs may cause the great decrease of the SERS activity of the substrate. The TEM observation showed that the freshly prepared colloidal Ag NPs were monodisperse spherical without any aggregation (Fig. 5a), and there was no oxygen signal peak in the EDS spectrum (inset of Fig. 5a). After the colloidal Ag NPs were stored for one week, a little aggregation was observed (Fig. 5b), being accompanied by the appearing of a weak oxygen signal peak in the EDS spectrum (inset of Fig. 5b). When the storing time was prolonged to four weeks, drastic morphological changes were observed for the colloidal Ag NPs: the particles coalesced into large aggregates with the development of irregular shapes (Fig. 5c), and an obviously oxygen peak was observed in the EDS spectrum (inset of Fig. 5c). The storing-time dependent increasing of the oxygen peak in intensity was only attributed to the oxidation of the metal NPs by the dissolved oxygen during the storing period. In contrast, the TEM observations of g-C_3N_4/Ag (Fig. 5(d and e)) confirmed that the Ag NPs were uniformly immobilized on the surface and edges of g-C_3N_4 sheets, and the long time storing did not induce any observable aggregation and oxidation of Ag NPs (inset of Fig. 5d). These observations solidly confirm that, unlike colloidal Ag NPs, g-C_3N_4/Ag hybrid substrates are both physically and chemically stable during the

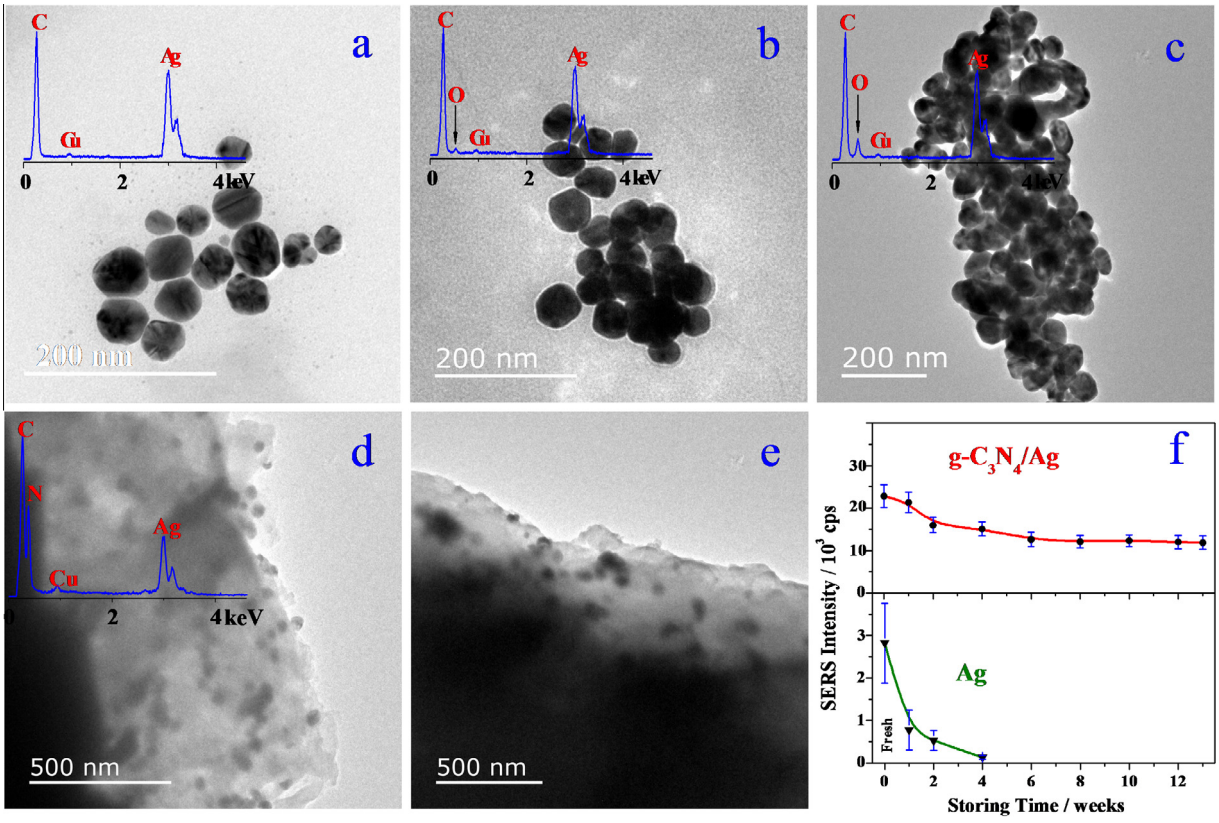

Fig. 5 – TEM images of Ag after being stored for different time periods of (a) fresh, (b) one week and (c) four weeks. TEM images of g-C_3N_4/Ag on different viewpoints: (d) up-bottom view and (e) side view. (f) The relationships between SERS intensity and storing time of substrate materials of Ag NPs and g-C_3N_4/Ag. The insets of (a–d) were corresponding EDS spectra. The peak intensity at 1619 cm^{-1} of CV was as a reference. (A colour version of this figure can be viewed online.)

long-term storing under ambient conditions. It ensures the good long-term stability of g-C_3N_4/Ag as a SERS substrate.

Indeed, by using the peak intensity of CV at 1619 cm^{-1} as a reference, the four-week storing caused a decrease of the SERS activity by more than 95.4% for the Ag NPs colloid, but only by 30.7% for the g-C_3N_4/Ag hybrid substrates, as shown in Fig. 5f. Each data is the average value recorded on 15 randomly selected points of one substrate. The RSD value for each group of the data was less than 10.1% for the g-C_3N_4/Ag hybrid substrates but and close to 47.4% for colloidal Ag NPs. For Ag colloids, the dramatic decrease of SERS intensity was attributed to the oxidation and aggregation of the Ag NPs, consistent with the results of TEM and EDS (Fig. 5(a–c)). As shown in Fig. 5f, in comparision with the Ag colloid, the observed SERS peak intensity on the g-C_3N_4/Ag hybrid substrate was only decreased slightly at the initial two weeks and then kept almost a constant for a long time period (more than 11 weeks) with a high peak intensity of about 12,000 cps (the peak at 1619 cm^{-1}), being 4–5 times that of the freshly-prepared Ag NPs colloid. This is because Ag NPs immobilized on the surface and edges of g-C_3N_4 sheets were less susceptible to oxidation.

It is well accepted that an N atom g-C_3N_4 can donate its lone pair of electrons to metal and that its 3d-orbitals could accept the d electrons of a transition metal in homogeneous catalysis [53]. A silver atom has $4d^{10}5s^1$ valence electron configuration [54]. The single-electron in the outermost layer of silver atom can easily be taken away by the oxidizing agent (such as O_2), as shown in Fig. 6a. The antioxidant ability of the Ag NPs immobilized on the surface and edges of g-C_3N_4 sheets could be explained in terms of the electron–donor effect of g-C_3N_4: electron-rich g-C_3N_4 donates its lone pair of electrons to silver surface through an interaction between Ag NPs and the N atoms in g-C_3N_4. When an oxidizing agent (O_2) outskirts the g-C_3N_4/Ag NPs hybrid, the negative charge of silver surface could transfer to the oxidizing agent, which will protect Ag NPs from oxidation. The process of charge transfer is shown in Fig. 6b.

Moreover, the electronic structure analysis of the interaction between g-C_3N_4 and Ag NPs (Fig. 7) showed that the most favorable interaction should occur between the HOMO of the electron donor (g-C_3N_4) and the LUMO of the electron acceptor (Ag NPs) because of the smallest energy gap between these two molecular orbitals. Here, cluster models including silver clusters with different sizes of Ag_n (n = 1–9) were used in the DFT computations to simulate the Ag NPs surface for optimizing the structures of surface complexes. To optimize the configurations and calculate HOMO and/or LUMO energy levels of g-C_3N_4–Ag_n, we studied the cluster effect on the calculation by utilizing a series of clusters containing various silver atoms (not shown here). We have found that the corresponding value did not change drastically upon varying the silver clusters size, being well consistent with the reported results [55]. Accordingly, a Ag_5 cluster was used in the present study to analyze the HOMO and/or LUMO energy levels of g-C_3N_4–Ag complex. For the interaction between Ag NPs and g-C_3N_4, the charge transfer is from the HOMO of g-C_3N_4 to the LUMO of silver cluster. Thus, the energies of the g-C_3N_4–Ag complex can be decreased, and the complex becomes quite stable after the coordination. This may further explain why the Ag NPs in the g-C_3N_4/Ag NPs hybrid could dramatically increase the stability. Therefore, the g-C_3N_4/Ag hybrid substrates possessed a long-term stability, which is of great importance for real-time SERS monitoring in practical applications.

The uniformity of g-C_3N_4/Ag hybrid substrate was evaluated by SERS mapping in this work, because the mapping

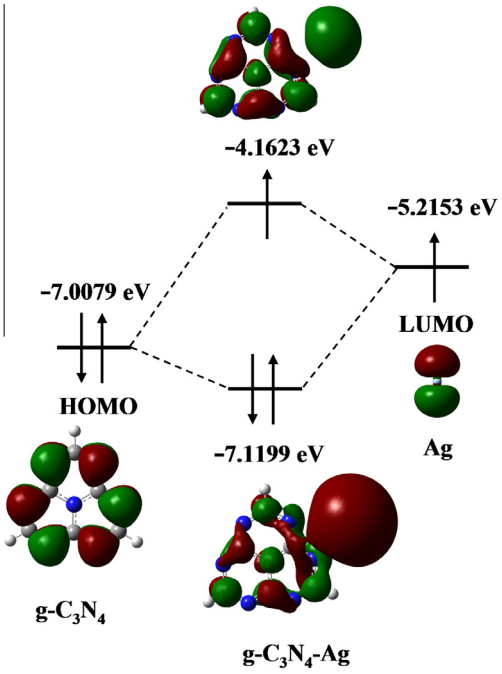

Fig. 7 – Frontier orbital theory analysis (B3LYP/Lanl2DZ, isocontour = 0.02) of coordination of g-C_3N_4 with Ag cluster. (A colour version of this figure can be viewed online.)

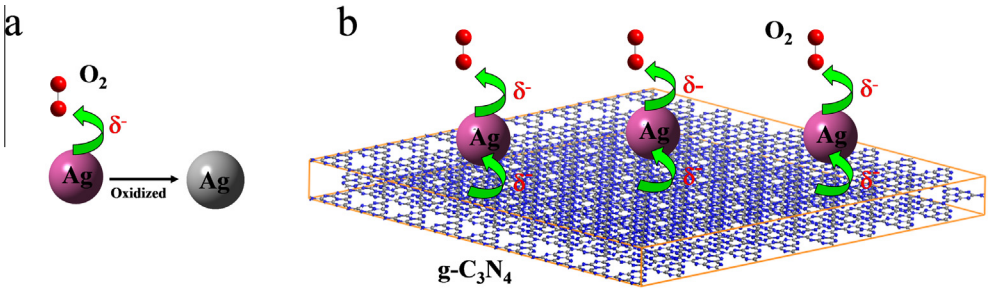

Fig. 6 – Schematic representation of the charge transfer between g-C_3N_4, O_2 and silver. The label δ^- means the negative charge of silver surface or g-C_3N_4. (A colour version of this figure can be viewed online.)

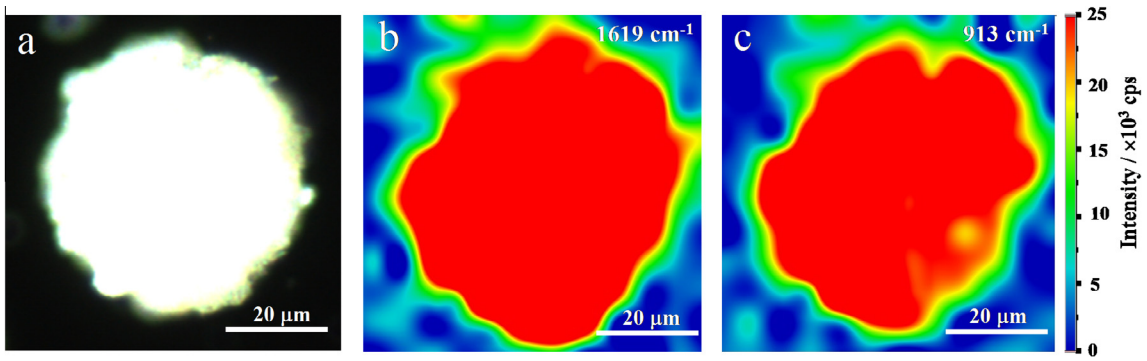

Fig. 8 – (a) Dark-field microscope image of the g-C_3N_4/Ag substrates in CV solution (2.5×10^{-6} mol L^{-1}). Raman *x*–*y* maps on the g-C_3N_4/Ag substrates by using the CV peak at (b) 1619 and (c) 913 cm^{-1}. Mapping measurements were carried out as raster scans in 4 μm steps over the specified area (about 60 μm × 60 μm) with 1 s integration time. The color scale bar is for (b) and (c). Scattering signals below a defined signal threshold, i.e., from places where there are no SERS signals, appear in dark blue. (A colour version of this figure can be viewed online.)

can reveal the localization and distribution of Raman probe molecules around the hot spots [10,56]. Fig. 8a showed a dark-field microscope image of the g-C_3N_4/Ag hybrid substrate by using CV as the probe. As illustrated in Fig. 8b, a SERS map with the intensity of the characteristic Raman CV peak at 1619 cm^{-1} shows the location of CV molecules on the corresponding area of the g-C_3N_4/Ag hybrid substrate. A SERS map of the characteristic CV peak at 913 cm^{-1} gave similar results (Fig. 8c). By comparing the optical microscope image (Fig. 8a), it was found that the area where the g-C_3N_4/Ag hybrid substrates exit almost entirely present red color (Fig. 8(b and c)). This confirmed that CV molecules were distributed uniformly around the hot spots. It also suggested that there was excellent uniformity on the g-C_3N_4/Ag hybrid substrates.

To check the adaptability of g-C_3N_4/Ag as a SERS substrate, other analytes were investigated, including Paraquat as a representative of pesticides, Guanine as a representative of small bio-molecules (see their chemical structures in Fig. S8 in SI). The Raman spectra of the solution samples of the used compounds were very weak in intensity, and hence they were not shown in the present work due to their almost invisible Raman signals. Instead, the Raman spectra of corresponding solid powders (Fig. 9, black lines) were used as the reference for the peak position in SERS measurement. In comparison with the Raman spectra of the solution samples with almost invisible Raman signals, the Raman signals of these substances were obviously enhanced on the hybrid substrate, as shown in Fig. 9 (blue lines). It was also observed that the Raman signals of g-C_3N_4/Ag hybrid substrate itself would not interfere with the determination of these analytes. In order to enhance the Raman scattering of the analyte by the SERS phenomenon, the analyte is required to be in very close proximity to the SERS substrate. If the analyte cannot remain in close proximity to the substrate through adsorption, SERS may not occur. There is no doubt that the SERS effect may be different for the different analytes such as CV, Paraquat and Guanine, due to the disparities within the adsorption properties, the distance and the interaction between these analytes and the g-C_3N_4/Ag hybrid substrate (especially, at the hot spots). The EFs were evaluated to be 1.9×10^5 and 6.6×10^7 for Paraquat and Guanine, respectively (Table S1 in SI). The significant EFs of the g-C_3N_4/Ag hybrid substrate toward different analytes indicate that it possesses wide adaptability as a SERS substrate.

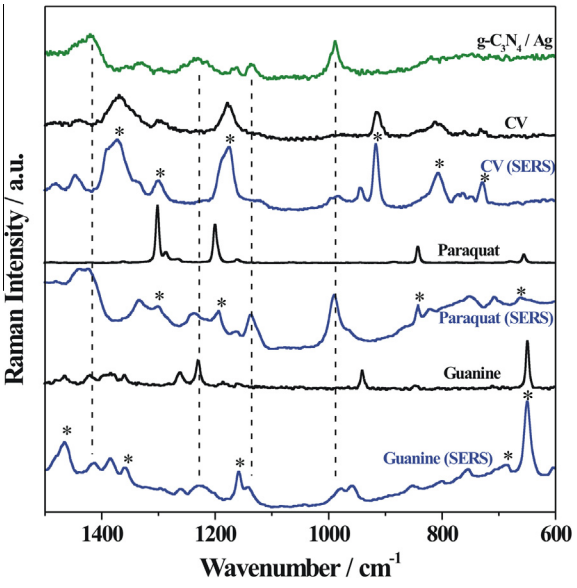

Fig. 9 – SERS spectra (blue lines) of CV (2.5×10^{-6} mol L^{-1}), Paraquat (1.0×10^{-3} mol L^{-1}) and Guanine (1.0×10^{-5} mol L^{-1}) on the g-C_3N_4/Ag hybrid substrates. The normal Raman spectra of g-C_3N_4/Ag hybrid substrates (olive line), CV powder, Paraquat powder and Guanine powder (black lines) were given for comparison. Peaks marked with an asterisk denoted the corresponding characteristic peaks of the target molecules in SERS. (A colour version of this figure can be viewed online.)

3.4. *A mechanism for SERS enhancement of g-C_3N_4/Ag NPs hybrid substrate*

To investigate the enhancement mechanism of g-C_3N_4/Ag NPs hybrid substrates, we first compared the UV–vis absorption spectra of Ag NPs, g-C_3N_4 and g-C_3N_4/Ag NPs (Fig. 10). A strong

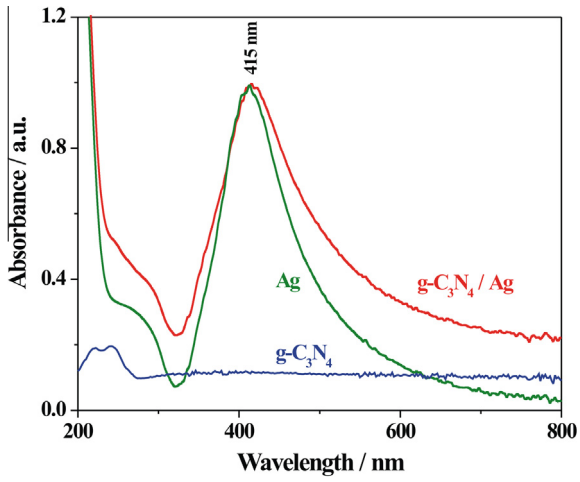

Fig. 10 – UV–vis absorption spectra of Ag NPs, g-C_3N_4 and g-C_3N_4/Ag. The absorption spectra of Ag NPs and g-C_3N_4/Ag were normalized by setting the peak absorbance be unit at 415 nm. The concentration of g-C_3N_4 was the same in the aqueous dispersions of g-C_3N_4 and g-C_3N_4/Ag for the measurement. (A colour version of this figure can be viewed online.)

absorption peak at 415 nm was observed in the UV–vis absorption spectrum of the colloidal Ag NPs, suggesting that the average diameter of the Ag NPs was about 40 nm [57], in accordance with the results of the particle size analysis and TEM. There was only weak absorption in the case of g-C_3N_4, but a strong absorption peak also occurred at 415 nm in the spectrum of g-C_3N_4/Ag NPs. It was noted that the absorption of g-C_3N_4/Ag NPs hybrid was considerably stronger than that of Ag NPs in the visible light region beyond 500 nm. It is known that when incident light illuminates a noble metal NP, it causes collective oscillations of the NP's surface electrons, which is termed surface plasmon resonance (SPR). Hence, the stronger absorption of g-C_3N_4/Ag NPs hybrid substrates will allow much easier occurrence of SPR. It should be noted that the SERS signals obtained on the substrate mainly come from the contribution of a propagating and localized surface plasmon effect induced by Ag NPs [58]. Liu and co-workers have directly confirmed the correlation between the SERS and SPR that captured simultaneously the SERS and SPR spectra [59]. When the incident laser with 532 nm illuminates the substrates, the Ag NPs immobilized on the surface and edges of g-C_3N_4 sheets will produce a greatly enhanced electromagnetic field than that of Ag NPs colloid. Meanwhile, there is a chemical enhancement from the charge transfer between Raman probe molecules and Ag NPs surface, as reported in our previous work [47].

Ling and co-workers [60,61] recently reported that there was a Raman enhancement on the surface of graphene and hexagonal boron nitride (h-BN) due to the chemical enhancement effect. As an analogue of graphene and h-BN, g-C_3N_4 itself could also possess a certain chemical enhancement. To understand it, we compared the normal Raman signal of CV in the solution (1.25×10^{-4} mol L^{-1}), SERS spectrum of CV on the surface of g-C_3N_4 (Fig. 11a), and the normal Raman of g-C_3N_4 (Figs. 3d and S8 in SI). Series of characteristic peaks of CV were observed in the normal Raman spectrum of CV solution. All of these peaks are significantly enhanced in intensity in the case of the SERS spectrum. Meanwhile, by comparing the Raman spectrum of g-C_3N_4 and SERS spectrum of CV on the surface of g-C_3N_4, the peaks at 1373, 1179 and 913 cm^{-1} with high-resolution were only observed in SERS spectrum of CV on the surface of g-C_3N_4, indicating that the enhanced spectrum of CV on the surface of g-C_3N_4 from the photoluminescence effect of g-C_3N_4 can be excluded. This demonstrates that there is a remarkable Raman enhancement effect on the surface of g-C_3N_4. In order to calculate the Raman EF, we chose the intensity of the Raman signals at 1373 cm^{-1}. It was found that the EF is about 4.5. Furthermore, the chemical enhancement of g-C_3N_4 was clarified by theoretical calculations. The Fermi level (E_F) of g-C_3N_4 and the LUMO and HOMO of the chemisorbed molecules (such

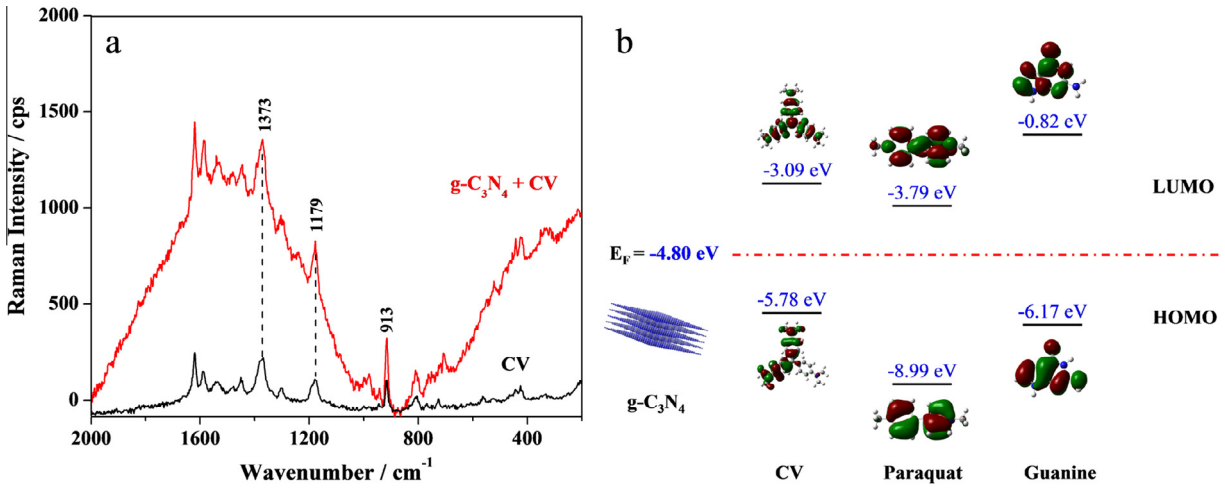

Fig. 11 – (a) SERS spectrum of CV (1.25×10^{-4} mol L^{-1}) on g-C_3N_4 and normal Raman spectrum of CV solution (1.25×10^{-4} mol L^{-1}), and (b) the relative HOMO and LUMO positions of the molecules in comparison with the Fermi level of g-C_3N_4. (A colour version of this figure can be viewed online.)

as CV, paraquat and guanine with structures shown in Fig. S9 in SI) were performance by CASTEP mode and DFT, respectively. Due to the π–π stacking, these aromatic molecules should lie parallel to the surface of g-C_3N_4. In addition, the position of the HOMO and LUMO of the molecules are all located on the two sides of the Fermi level of g-C_3N_4 (Fig. 11b). These observations suggest that charge transfer can easily occur between g-C_3N_4 and the adsorbed molecules, which will induce chemical enhancement. Like h-BN, because g-C_3N_4 has a strong C–N bond, and the dipole–dipole coupling may occur [61]. This interface dipole–dipole interaction could induce a significant Raman enhancement. Hence it was concluded that both the electromagnetic and chemical enhancement originated from Ag NPs immobilized on the surface and edges of g-C_3N_4 sheets and the intrinsic chemical enhancement of g-C_3N_4 contribute to the total SERS enhancement for g-C_3N_4/Ag NPs hybrid substrates.

3.5. *Interaction between g-C_3N_4 and Ag*

Raman, photoluminescence and XPS N 1s spectra of different substrates were acquired to further study the interaction between Ag NPs and g-C_3N_4 (Fig. 12). No observable Raman signals were detected on either Ag NPs colloid or g-C_3N_4, but a clear Raman spectrum was obtained on g-C_3N_4/Ag (Fig. 12a). Several characteristic peaks in the spectrum of g-C_3N_4/Ag were analyzed here. The peaks at 1585 and 557 cm^{-1} are rooted from the enhancement Raman of g-C_3N_4 and the corresponding vibrational assignments were calculated by the CASTER code (Fig. S10 in SI). The band at 1585 cm^{-1} is attributable to C=N stretching vibration of g-C_3N_4, which is also defined as the graphitic G band, indicating the formation of graphitic structure. The peak at 557 cm^{-1} is assigned in-plane symmetrical stretching vibration of heptazine heterocycles [45]. In comparison with the spectrum of g-C_3N_4, the appearance of the two peaks can be attributed to the SERS effect of Ag NPs. Moreover, in the spectrum of g-C_3N_4/Ag, there was a peak at 221 cm^{-1}, which is attributed to the N-Ag symmetric stretching mode, in accordance with the reported results [47]. Its appearing indicates that there is an interaction between Ag and g-C_3N_4 through the N-Ag bonding [53].

The photoluminescence spectrum of g-C_3N_4 in aqueous dispersion was measured. When the excitation wavelength changed from 300 to 380 nm, the photoluminescence spectra were almost invariable and showed a strong peak at 437 nm, indicating that g-C_3N_4 exhibited an excitation-independent photoluminescence behavior [62]. As illustrated in Fig. 12b, when the dispersion was excited at 316 nm, a peak at 356 nm, with respect to the Raman scattered signal from water molecules (~3652 cm^{-1}) [63,64] was observed in all photoluminescence spectra. The Ag NPs colloid showed a weak photoluminescence peak centered at 456 nm. This could be explained as follows: electrons from occupied d bands were excited into states above the Fermi level, subsequent electron-phonon and hole-phonon scattering processes led to energy loss, and finally photoluminescent recombination of an electron from an occupied sp band with the hole occurred [65,66]. Both g-C_3N_4 and g-C_3N_4/Ag NPs presented a strong peak at 437 nm, but the presence of Ag NPs caused

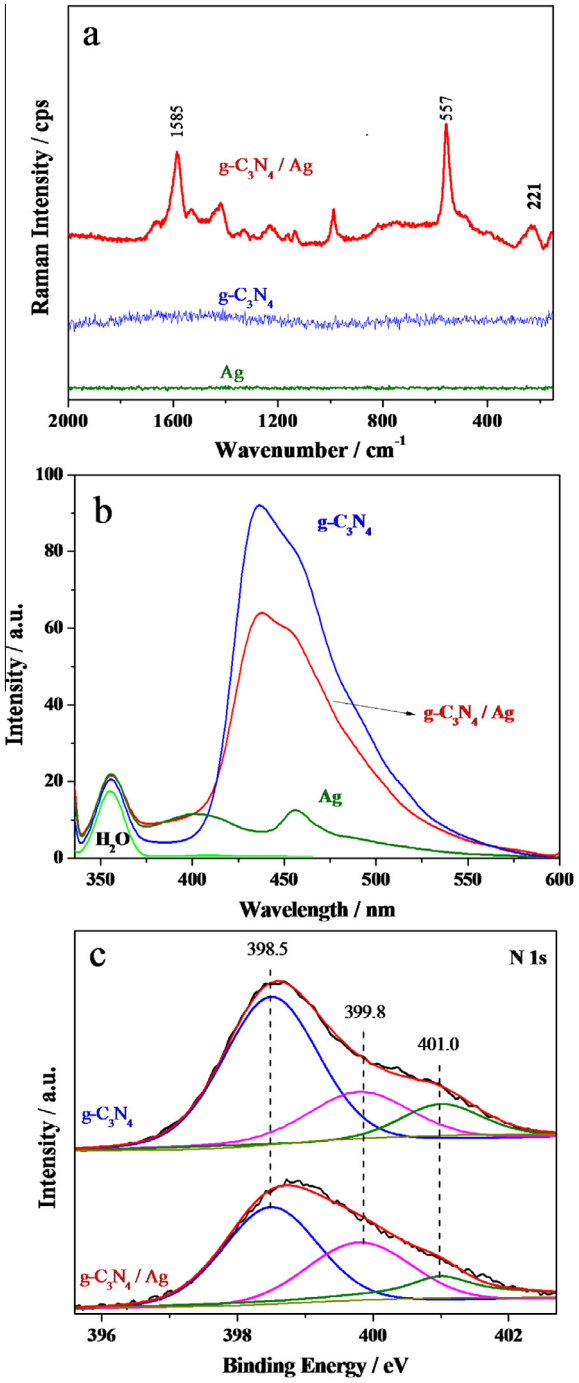

Fig. 12 – (a) Raman and (b) photoluminescence spectra of Ag NPs, g-C_3N_4, g-C_3N_4/Ag and H_2O, and (c) N 1s XPS spectra of g-C_3N_4 and g-C_3N_4/Ag. In the photoluminescence measurement, the concentration of g-C_3N_4 was the same in the aqueous dispersion of g-C_3N_4 and g-C_3N_4/Ag. (A colour version of this figure can be viewed online.)

a considerable decrease of photoluminescence of g-C_3N_4 in intensity. This quenching effect also implies that there is an interaction between Ag NPs and g-C_3N_4 (through N atoms) [67].

Fig. 12(c) compared the XPS N1s envelops of g-C_3N_4 and g-C_3N_4/Ag NPs, which could be deconvoluted into three peaks at

398.5, 399.8 and 401.0 eV, being assigned to sp^2-hybridized N (C–N–C), sp^3-hybridized N (N–C]$_3$) and amino functional groups with a hydrogen atom (C–NH), respectively [62]. It was found that the intensity ratio of N(sp^2)/N(sp^3) decreased from 2.6 to 1.6 after the Ag NPs grown on g-C_3N_4 (Table S2 in SI). This was attributed to the η^1 and η^2 coordination of Ag NPs to g-C_3N_4 and/or the consequence of the silver–π interaction [68,69], causing that some sp^2-hybridized nitrogen atoms tend to the sp^3-hybridized form in heptazine heterocycles after g-C_3N_4 interacts with Ag NPs in the g-C_3N_4/Ag NPs hybrid. Hence, the decreased N(sp^2)/N(sp^3) ratio in the XPS N 1s profiles further confirmed the interaction between Ag NPs and g-C_3N_4. It is concluded that due to the strong interaction between Ag NPs and g-C_3N_4, the hybrid can uniformly immobilize Ag NPs on the surface and edges of g-C_3N_4 sheets to protect Ag NPs from oxidation, ensuring the long-term stability of the hybrid during its storing under ambient conditions.

4. Conclusion

We have successfully developed g-C_3N_4/Ag NPs hybrid materials as SERS substrates with good long-term stability and high SERS performance. The hybrid substrates were used to enrich the analytes due to the high affinity of g-C_3N_4 to aromatic molecules, and the immobilized Ag NPs in the hybrid could supply strong SERS enhancement. In addition, 4.5 times enhanced SERS intensities were detected from the g-C_3N_4 itself. The g-C_3N_4/Ag NPs substrates exhibited a remarkable Raman enhancement effect for CV with an enhancement factor of 4.6×10^8. The interaction between Ag NPs and g-C_3N_4 was studied by using SERS, TEM–EDS, XPS, and DFT calculations. It was suggested that the Ag NPs could uniformly immobilize on the surface and edges of g-C_3N_4 sheets to prevent oxidation, ensuring the long-term stability of the hybrid during its storing in practical applications. The g-C_3N_4/Ag NPs hybrid substrates also exhibited excellent reproducibility, uniformity and broad adaptability. This is the first report of SERS in carbon nitride materials field and therefore it extends the scope of future applications of carbon nitride.

Acknowledgments

This work was financially supported by the National High Technology Research and Development Program of China (863 Program) (Grant No. 2012AA06A304), the National Science Foundation of China (Grant Nos. 21177044, 21377169 and 21471122), and the Scientific Research Key Project of Hubei Provincial Department of Education (China) (Project No. D20121503) and the Natural Science Foundation of Hubei Province (China) (Grant No. 2012FFB04702).

Appendix A. Supplementary data

Supplementary data associated with this article can be found, in the online version, at http://dx.doi.org/10.1016/j.carbon.2015.02.025.

REFERENCES

[1] Chen S, Li X, Zhao Y, Chang L, Qi J. Graphene oxide shell-isolated Ag nanoparticles for surface-enhanced Raman scattering. Carbon 2015;81:767–72.
[2] Prado E, Colin A, Servant L, Lecomte S. SERS Spectra of oligonucleotides as fingerprints to detect labelfree RNA in microfluidic devices. J Phys Chem C 2014;118:13965–71.
[3] Chang TW, Seo S, Jin H, Wang X, Liu GL. Comparison of surface-enhanced Raman spectroscopy on absorbing and nonabsorbing nanostructured substrates. J Phys Chem C 2014;118:18693–9.
[4] Fleischmann M, Hendra PJ, McQuillan AJ. Raman-spectra of pyridine adsorbed at a silver electrode. Chem Phys Lett 1974;26:163–6.
[5] Nergiz SZ, Gandra N, Farrell ME, Tian L, Pellegrino PM, Singamaneni S. Biomimetic SERS substrate: peptide recognition elements for highly selective chemical detection in chemically complex media. J Mater Chem A 2013;1:6543–9.
[6] Hatab NA, Eres G, Hatzinger PB, Gu BH. Detection and analysis of cyclotrimethylenetrinitramine (RDX) in environmental samples by surface-enhanced Raman spectroscopy. J Raman Spectrosc 2010;41:1131–6.
[7] Betz JF, Cheng Y, Rubloff GW. Direct SERS detection of contaminants in a complex mixture: rapid, single step screening for melamine in liquid infant formula. Analyst 2012;137:826–8.
[8] Zhang Y, Huan Y, Zhai F, Du R, Lai K. Analyses of enrofloxacin, furazolidone and malachite green in fish products with surface-enhanced Raman spectroscopy. Food Chem 2012;135:845–50.
[9] Wang Y, Yan B, Chen L. SERS tags: novel optical nanoprobes for bioanalysis. Chem Rev 2013;113:1391–428.
[10] Maiti KK, Dinish US, Samanta A, Vendrell M, Soh K-S, Park S-J, et al. Multiplex targeted in vivo cancer detection using sensitive near-infrared SERS nanotags. Nano Today 2012;7:85–93.
[11] Wustholz KL, Brosseau CL, Casadio F, Van Duyne RP. Surface-enhanced Raman spectroscopy of dyes: from single molecules to the artists' canvas. Phys Chem Chem Phys 2009;11:7350–9.
[12] Wang R, Chen Y, Chen S, Chang Y. Unusual functionalization of reduced graphene oxide for excellent chemical surface-enhanced Raman scattering by coupling with ZnO. Carbon 2014;70:215–23.
[13] Kneipp K, Kneipp H, Kneipp J. SERS in local optical fields of silver and gold nanoaggregates: from single-molecule Raman spectroscopy to ultrasensitive probing in live cells. Acc Chem Res 2006;39:443–50.
[14] Campion A, Ivanecky JE, Child CM, Foster M. On the mechanism of chemical enhancement in surface-enhanced Raman scattering. J Am Chem Soc 1995;117:11807–8.
[15] Jeanmaire DL, Van Duyne RP. Surface Raman spectroelectrochemistry: part I. heterocyclic, aromatic, and aliphatic amines adsorbed on the anodized silver electrode. J Electroanal Chem 1977;84:1–20.
[16] Albrecht MG, Creighton JA. Anomalously intense Raman spectra of pyridine at a silver electrode. J Am Chem Soc 1977;99:5215–7.
[17] Nickel U, Castell AZ, Poppl K, Schneider S. A silver colloid produced by reduction with hydrazine as support for highly sensitive surface-enhanced Raman spectroscopy. Langmuir 2000;16:9087–91.
[18] Novoselov KS, Geim AK, Morozov SV, Jiang D, Zhang Y, Dubonos SV, et al. Electric field effect in atomically thin carbon films. Science 2004;306:666–9.

[19] Cittadini M, Bersani M, Perrozzi F, Ottaviano L, Wlodarski W, Martucci A. Graphene oxide coupled with gold nanoparticles for localized surface plasmon resonance based gas sensor. Carbon 2014;69:452–9.
[20] Liu ZM, Guo ZY, Zhong HQ, Qin XC, Wan MM, Yang BW. Graphene oxide based surface-enhanced Raman scattering probes for cancer cell imaging. Phys Chem Chem Phys 2013;15:2961–6.
[21] Li SK, Yan YX, Wang JL, Yu SH. Bio-inspired in situ growth of monolayer silver nanoparticles on graphene oxide paper as multifunctional substrate. Nanoscale 2013;5:12616–23.
[22] Huang J, Zhang L, Chen B, Ji N, Chen F, Zhang Y, et al. Nanocomposites of size-controlled gold nanoparticles and graphene oxide: formation and applications in SERS and catalysis. Nanoscale 2010;2:2733–8.
[23] Qin Y, Li J, Kong Y, Li X, Tao Y, Li S, et al. In situ growth of Au nanocrystals on graphene oxide sheets. Nanoscale 2014;6:1281–5.
[24] Saha A, Palmal S, Jana NR. Highly reproducible and sensitive surface-enhanced Raman scattering from colloidal plasmonic nanoparticle via stabilization of hot spots in graphene oxide liquid crystal. Nanoscale 2012;4:6649–57.
[25] Fan W, Lee YH, Pedireddy S, Zhang Q, Liu T, Ling XY. Graphene oxide and shape-controlled silver nanoparticle hybrids for ultrasensitive single-particle surface-enhanced Raman scattering (SERS) sensing. Nanoscale 2014;6:4843–51.
[26] Gupta VK, Atar N, Yola ML, Eryılmaz M, Torul H, Tamer U, et al. A novel glucose biosensor platform based on Ag@AuNPs modified graphene oxide nanocomposite and SERS application. J Colloid Interface Sci 2013;406:231–7.
[27] Li X, Li J, Zhou X, Ma Y, Zheng Z, Duan X, et al. Silver nanoparticles protected by monolayer graphene as a stabilized substrate for surface enhanced Raman spectroscopy. Carbon 2014;66:713–9.
[28] Xu H, Yan J, She XJ, Xu L, Xia JX, Xu YG, et al. Graphene-analogue carbon nitride: novel exfoliation synthesis and its application in photocatalysis and photoelectrochemical selective detection of trace amount of Cu^{2+}. Nanoscale 2014;6:1406–15.
[29] Liebig J. About some nitrogen compounds. Ann Pharm 1834;10:10.
[30] Wang X, Blechert S, Antonietti M. Polymeric graphitic carbon nitride for heterogeneous photocatalysis. ACS Catal 2012;2:1596–606.
[31] She XJ, Xu H, Xu YG, Yan J, Xia JX, Xu L, et al. Exfoliated graphene-like carbon nitride in organic solvents: enhanced photocatalytic activity and highly selective and sensitive sensor for the detection of trace amounts of Cu^{2+}. J Mater Chem A 2014;2:2563–70.
[32] Kawaguchi M, Yagi S, Enomoto H. Chemical preparation and characterization of nitrogen-rich carbon nitride powders. Carbon 2004;42:345–50.
[33] Liu AY, Cohen ML. Prediction of new low compressibility solids. Science 1989;245:841–2.
[34] Kroke E, Schwarz M. Novel group 14 nitrides. Coord Chem Rev 2004;248:493–532.
[35] Chen X, Jun Y, Takanabe K, Maeda K, Domen K, Fu X, et al. Ordered mesoporous SBA-15 type graphitic carbon nitride: a semiconductor host structure for photocatalytic hydrogen evolution with visible light. Chem Mater 2009;21:4093–5.
[36] Shalom M, Gimenez S, Schipper F, Herraiz-Cardona I, Bisquert J, Antonietti M. Controlled carbon nitride growth on surfaces for hydrogen evolution electrodes. Angew Chem 2014;126:3728–32.
[37] Hong ZH, Shen B, Chen YL, Lin BZ, Gao BF. Enhancement of photocatalytic H_2 evolution over nitrogen-deficient graphitic carbon nitride. J Mater Chem A 2013;1:11754–61.
[38] Li Q, Yang J, Feng D, Wu Z, Wu Q, Park SS, et al. Facile synthesis of porous carbon nitride spheres with hierarchical three-dimensional mesostructures for CO_2 capture. Nano Res 2010;3:632–42.
[39] Li X, Chen J, Wang X, Sun J, Antonietti M. Metal-free activation of dioxygen by graphene/g-C_3N_4 nanocomposites: functional dyads for selective oxidation of saturated hydrocarbons. J Am Chem Soc 2011;133:8074–7.
[40] Thomas A, Fischer A, Goettmann F, Antonietti M, Müller JO, Schlögl R. Graphitic carbon nitride materials: variation of structure and morphology and their use as metal-free catalysts. J Mater Chem 2008;18:4893–908.
[41] Oh J, Lee S, Zhang K, Hwang JO, Han J, Park G, et al. Graphene oxide-assisted production of carbon nitrides using a solution process and their photocatalytic activity. Carbon 2014;66:119–25.
[42] Wang YJ, Bai XJ, Pan CS, He J, Zhu YF. Enhancement of photocatalytic activity of Bi_2WO_6 hybridized with graphite-like C_3N_4. J Mater Chem 2012;22:11568–73.
[43] Zhang L, Jing DW, She XL, Liu HW, Yang DJ, Lu Y, et al. Heterojunctions in g-C_3N_4/TiO_2(B) nanofibres with exposed (001) plane and enhanced visible-light photoactivity. J Mater Chem A 2014;2:2071–8.
[44] Tian J, Liu Q, Ge C, Xing Z, Asiri AM, Al-Youbi AO, et al. Ultrathin graphitic carbon nitride nanosheets: a low-cost, green, and highly efficient electrocatalyst toward the reduction of hydrogen peroxide and its glucose biosensing application. Nanoscale 2013;5:8921–4.
[45] Jiang JZ, Ou-yang L, Zhu LH, Zheng AM, Zou J, Yi XF, et al. Dependence of electronic structure of g-C_3N_4 on the layer number of its nanosheets: a study by Raman spectroscopy coupled with first-principles calculations. Carbon 2014;80:213–21.
[46] Xu J, Zhang LW, Shi R, Zhu YF. Chemical exfoliation of graphitic carbon nitride for efficient heterogeneous photocatalysis. J Mater Chem A 2013;1:14766–72.
[47] Jiang JZ, Ou-Yang L, Zhu LH, Zou J, Tang HQ. Novel one-pot fabrication of lab-on-a-bubble@Ag substrate without coupling-agent for surface enhanced Raman scattering. Sci Rep 2014;4. 3942(1–9).
[48] Frisch MJ, Trucks GW, Schlegel HB, Scuseria GE, Robb MA, Cheeseman JR, et al. Gaussian 09, Revision C. 01. Wallingford CT: Gaussian Inc.; 2010.
[49] Segall MD, Lindan PJD, Probert MJ, Pickard CJ, Hasnip PJ, Clark SJ, et al. First-principles simulation: ideas, illustrations and the CASTEP code. J Phys: Condens Matter 2002;14:2717–44.
[50] Ceperley DM, Alder BJ. Ground state of the electron gas by a stochastic method. Phys Rev Lett 1980;45:566–9.
[51] Lu G, Li H, Liusman C, Yin Z, Wu S, Zhang H. Surface enhanced Raman scattering of Ag or Au nanoparticle-decorated reduced graphene oxide for detection of aromatic molecules. Chem Sci 2011;2:1817–21.
[52] Chen T, Du C, Tan LH, Shen Z, Chen H. Site-selective localization of analytes on gold nanorod surface for investigating field enhancement distribution in surface-enhanced Raman scattering. Nanoscale 2011;3:1575–81.
[53] Hu G, Feng Z, Li J, Jia G, Han D, Liu Z, et al. Adsorption of ethanediamine on colloidal silver: a surface-enhanced Raman spectroscopy study combined with density functional theory calculations. J Phys Chem C 2007;111:11267–74.
[54] Hu G, Feng Z, Han D, Li J, Jia G, Shi J, et al. Charge transfer between triphenyl phosphine and colloidal silver: a SERS study combined with DFT calculations. J Phys Chem C 2007;111:8632–7.
[55] Wang A, Huang Y, Sur UK, Wu D, Ren B, Rondinini S, et al. In situ identification of intermediates of benzyl chloride reduction at a silver electrode by SERS coupled with DFT calculations. J Am Chem Soc 2010;132:9534–6.

[56] Pallaoro A, Braun GB, Reich NO, Moskovits M. Mapping local pH in live cells using encapsulated fluorescent SERS nanotags. Small 2010;6:618–22.
[57] Chen B, Jiao X, Chen D. Size-controlled and size-designed synthesis of nano/submicrometer Ag particles. Cryst Growth Des 2010;10:3378–86.
[58] Liu Y, Xu S, Li H, Jian X, Xu W. Localized and propagating surface plasmon co-enhanced Raman spectroscopy based on evanescent field excitation. Chem Commun 2011;47:3784–6.
[59] Liu Y, Xu S, Tang B, Wang Y, Zhou J, Zheng X, et al. Simultaneous measurement of surface plasmon resonance and surface-enhanced Raman scattering. Rev Sci Instrum 2010;81. 036105(1–3).
[60] Ling X, Xie L, Fang Y, Xu H, Zhang H, Kong J. Can graphene be used as a substrate for Raman enhancement? Nano Lett 2010;10:553–61.
[61] Ling X, Fang W, Lee YH, Araujo PT, Zhang X, Rodriguez-Nieva JF. Raman enhancement effect on two-dimensional layered materials: graphene, h-BN and MoS_2. Nano Lett 2014;14:3033–40.
[62] Zhang S, Li J, Zeng M, Xu J, Wang X, Hu W. Polymer nanodots of graphitic carbon nitride as effective fluorescent probes for the detection of Fe^{3+} and Cu^{2+} ions. Nanoscale 2014;6:4157–62.
[63] Walrafen GE. Raman spectral studies of water structure. J Chem Phys 1964;40:3249–56.
[64] Ahmad SR, Reynolds DM. Monitoring of water quality using fluorescence technique: prospect of on-line process control. Water Res 1999;33:2069–74.
[65] Apell P, Monreal R, Lundqvist S. Photoluminescence of noble metals. Phys Scr 1988;38:174–9.
[66] Wu WT, Zhou T, Zhou SQ. Tunable photoluminescence of Ag nanocrystals in multiple-sensitive hybrid microgels. Chem Mater 2009;21:2851–61.
[67] Tian J, Liu Q, Asiri AM, Al-Youbi AO, Sun X. Ultrathin graphitic carbon nitride nanosheet: a highly efficient fluorosensor for rapid, ultrasensitive detection of Cu^{2+}. Anal Chem 2013;85:5595–9.
[68] Olmstead MM, Maitra K, Balch AL. Formation of a curved silver nitrate network that conforms to the shape of C_{60} and encapsulates the fullerene-structural characterization of $C_{60}\{Ag(NO_3)\}_5$. Angew Chem Int Ed 1999;38:231–3.
[69] Munakata M, Wu LP, Ning GL, Kuroda-Sowa T, Maekawa M, Suenaga Y, et al. Construction of metal sandwich systems derived from assembly of silver(I) complexes with polycyclic aromatic compounds. J Am Chem Soc 1999;121:4968–76.